

# THE DOMINANCE OF NEUTRINO-DRIVEN CONVECTION IN CORE-COLLAPSE SUPERNOVAE

JEREMIAH W. MURPHY<sup>1</sup>, JOSHUA C. DOLENCE<sup>1</sup>, AND ADAM BURROWS<sup>1</sup>

*Draft version March 4, 2013*

## ABSTRACT

Multi-dimensional instabilities have become an important ingredient in core-collapse supernova (CCSN) theory. Therefore, it is necessary to understand the driving mechanism of the dominant instability. Comparing 3D CCSN simulations with turbulence theory, we find that buoyancy-driven convection dominates post-shock turbulence. In general, the convective fluxes and kinetic energies in the neutrino-heated region are consistent with expectations of buoyancy-driven convection. Specifically, the convective flux is positive where buoyancy actively drives convection, and the radial and tangential components of the kinetic energy are in rough equipartition (i.e.  $K_r \sim K_\theta + K_\phi$ ). Both results are natural consequences of buoyancy-driven convection, and are commonly observed in simulations of convection in other contexts. Most compelling, though, is the consistency between 3D CCSN simulations and predictions of neutrino-driven convection theory. For one, global buoyant driving is balanced by global turbulent dissipation. Secondly, the convective luminosity and turbulent dissipation are linearly proportional to the driving neutrino power. Thirdly, we accurately calculate the shock radius only if we include turbulent ram pressure in the shock conditions. In all, these results suggest that in neutrino-driven explosions the multi-dimensional motions are consistent with neutrino-driven convection, and there is little need to invoke alternative instabilities such as the standing accretion shock instability.

*Subject headings:* convection — hydrodynamics — instabilities — methods: analytical — methods: numerical — shock waves — supernovae: general — turbulence

## 1. INTRODUCTION

The explosive death of massive stars, in particular core-collapse supernovae (CCSNe), are some of the most energetic explosions in the Universe, and, as such, are fundamental to a wide range of other astrophysical phenomena. To highlight a few important examples, CCSNe are a major site for nucleosynthesis, mark the birth of neutron stars and black holes, and are major contributors to galactic dynamics and star formation. Despite their importance, understanding the mechanism remains an important unsolved problem. Whatever the mechanism, it has long been suggested that neutrinos and multi-dimensional instabilities play major, if not central, roles (Epstein 1979; Bethe & Wilson 1985; Burrows 1987; Wilson & Mayle 1988; Bethe 1990; Herant et al. 1992; Benz et al. 1994; Herant et al. 1994; Burrows et al. 1995; Janka & Müller 1995; Blondin et al. 2003; Marek & Janka 2007; Murphy & Burrows 2008; Nordhaus et al. 2010). In this paper, we use turbulence theory to show that the dominant multi-dimensional instability is consistent with neutrino-driven buoyant convection.

Multi-dimensional simulations have long suggested that aspherical, nonlinear instabilities play important roles in aiding the delayed-neutrino mechanism toward successful explosions. Otherwise, except for the least massive stars (Kitaura et al. 2006; Burrows et al. 2007), the spherical delayed-neutrino mechanism fails to produce explosions (Liebendörfer et al. 2001b,a; Rampp & Janka 2002; Buras et al. 2003; Thompson et al. 2003; Liebendörfer et al. 2005). Even though the importance of multi-dimensionality is clear, which instability dominates the aspherical motions has been less clear. Initially, neutrino-driven convection was identified as the most relevant multidimensional instability (Burrows 1987; Wilson & Mayle 1988; Bethe 1990;

Benz et al. 1994; Burrows et al. 1995; Janka & Müller 1995), but then idealized 2D simulations discovered a new instability, the standing accretion shock instability (SASI) (Blondin et al. 2003). Both must exist at some level, but it has never been made clear which dominates in realistic simulations.

Investigating the importance of neutrino-driven convection in CCSN theory has a long history. In the earliest investigations, it was suggested that convection expands the shock radius, making the gain region larger and increasing net neutrino heating (Benz et al. 1994; Burrows et al. 1995; Janka & Müller 1995, 1996). However, none of these investigations verified that the aspherical motions are in fact due to neutrino-driven convection, nor did they check whether the turbulent ram pressure is actually sufficient to produce the expanded radius. More recently, Murphy & Burrows (2008) considered the global conditions for explosion and found that turbulence reduces the critical neutrino luminosity for successful explosions (see Yamasaki & Yamada (2006) and Murphy & Meakin (2011) for theoretical discussions). Using 3D simulations, Nordhaus et al. (2010) found similar results, but Hanke et al. (2011) conclude that another multi-dimensional instability, the SASI, might be more important in aiding successful explosions.

The SASI is an instability of the standing accretion shock that was first discovered in idealized simulations which purposely neglected neutrinos to suppress convective instabilities (Blondin et al. 2003). These idealized 2D simulations exhibited strong up-and-down sloshing motions of the shock, leading to an immediate connection to the sloshing shock motions observed in more realistic 2D simulations. Consequently, most subsequent studies focused on the mechanism responsible for the SASI or postulated that the SASI could lead to successful explosions (Blondin et al. 2003; Blondin & Mezzacappa 2006; Foglizzo et al. 2006; Marek & Janka 2007; Scheck et al. 2008; Foglizzo 2009; Sato et al. 2009; Fernández 2010; Hanke et al. 2011). Linear

<sup>1</sup> Princeton University, jmurphy@astro.princeton.edu, jdolence@astro.princeton.edu, burrows@astro.princeton.edu

theory suggests that an advective-acoustic cycle is the mechanism for the SASI (Guilet & Foglizzo 2012; Foglizzo et al. 2012). These analyses show that under certain conditions an advective-acoustic instability in addition to the buoyant instability may operate in the core collapse context. However, to more easily study the SASI, most analyses used idealized simulations in which buoyancy-driven instabilities were suppressed (Blondin et al. 2003; Blondin & Mezzacappa 2006; Sato et al. 2009; Foglizzo 2009).

Studies that focus on the SASI and include neutrino transport or heating are few (Foglizzo et al. 2006; Scheck et al. 2008; Fernández & Thompson 2009). Using a toy model and linear theory, Foglizzo et al. (2006) considered the linear growth of convective instabilities and found that advection can sweep small-perturbation modes out of the convectively unstable region before they have time to grow to nonlinear amplitudes. Hence, they conclude that a negative entropy gradient is not enough to drive convective instability; one must also consider the ratio of the advection time to the local buoyancy timescale ( $\chi$ ). For  $\chi > 3$ , the linear convective instability succeeds, but for  $\chi < 3$ , the SASI dominates. However, Foglizzo et al. (2006) cautioned that this analysis is best suited for linear growth of small perturbations, and if the seed perturbations are sufficiently large, convection may ensue even if  $\chi < 3$ . Scheck et al. (2008) investigated whether this condition is relevant in more realistic simulations and found that with small initial perturbations, the SASI initially appeared to dominate when  $\chi < 3$ . However, after  $\sim 100$  ms, large SASI perturbations appeared to trigger convection. With larger, but still modest initial perturbations  $\mathcal{O}(10^{-2}v_r)^2$ , convection appeared to dominate at all times. Given that large convective perturbations in the progenitor (Bazan & Arnett 1998; Meakin & Arnett 2007) will provide large perturbative seeds, the latter scenario is more likely. Based upon the linear analysis, Foglizzo et al. (2006) conclude that “advective stabilization weakens the influence of convection on the largest modes,” but we suggest that the multi-dimensional simulations indicate otherwise.

In many other simulations, there are hints that buoyancy-driven convection dominates nonlinear motions. Two-dimensional and three-dimensional simulations that include neutrinos show prominent, positively-buoyant, high-entropy plumes and negatively-buoyant, low-entropy plumes at late times (see Figure 1). Even in 2D simulations that exhibit large sloshing motions of the shock, outward excursions of the shock are accompanied by rising, high-entropy plumes. Most recently Burrows et al. (2012) have analyzed the multi-dimensional shock motions in 2D and 3D simulations and have found that the sloshing motions frequently identified with SASI are suppressed in 3D compared to 2D, and the character of the oscillations is sensitive to the driving neutrino luminosity. These results are consistent with neutrino-driven convection as the source for the aspherical shock motions. The correlation with neutrino luminosity is an obvious indicator of neutrino-driven convection. The reduction in the large-scale sloshing modes in going from 2D to 3D is consistent with known differences in turbulence between 2D and 3D (Boffetta & Ecke 2012). In 3D, turbulence cascades to smaller scales only via a constant energy cascade. Two-dimensional turbulence exhibits a double cascade: an enstrophy cascade to smaller scales and an energy cascade to larger scales. This difference naturally leads to more large-scale,

coherent structures in 2D (see Figure 1). Might this be the source for the apparent sloshing modes in realistic 2D simulations? Albeit circumstantial, these observations call into question the assumed dominance of a SASI in CCSN simulations that include neutrinos.

Determining which instability dominates, requires a detailed analysis of the nonlinear motions and comparisons with theoretical predictions. Unfortunately, a nonlinear theory for a SASI mechanism does not yet exist, so the predictions of such a theory can not be falsified. On the other hand, nonlinear theories for buoyancy-driven convection do exist, and can be tested against simulations that include neutrinos and a realistic equation of state. In this paper, we focus on the latter and leave the former for future work.

To test whether nonlinear, turbulent flows of 3D CCSN simulations are consistent with buoyancy-driven convection, we compare these simulations with a nonlinear theory for neutrino-driven convection (Murphy & Meakin 2011). In section 2, we describe the 3D simulations. Then in section 3, we highlight some of the more illuminating elements of the nonlinear convection theory, and in section 4, we compare the predictions of this theory with the properties of the 3D simulations. Finally, in section 5, we conclude that the turbulent motions in 3D simulations are consistent with buoyancy-driven convection.

## 2. SIMULATIONS

The numerical results of this paper are based upon CCSN simulations using CASTRO and are similar to the simulations of Nordhaus et al. (2010). CASTRO solves the hydrodynamics equations using a Godunov-type finite-volume scheme where the boundary fluxes are calculated using an approximate Riemann solver (Almgren et al. 2010). Specifically, it evolves the conservative hydrodynamic equations:

$$\partial_t \rho + \nabla \cdot (\rho \mathbf{u}) = 0, \quad (1)$$

$$\partial_t (\rho \mathbf{u}) + \nabla \cdot (\rho \mathbf{u} \mathbf{u}) = -\nabla P + \rho \mathbf{g}, \quad (2)$$

and

$$\partial_t (E) + \nabla \cdot [\mathbf{u}(E + P)] = \rho \mathbf{u} \cdot \mathbf{g} + \rho q, \quad (3)$$

where  $\rho$  is the mass density,  $\mathbf{u}$  is the velocity,  $\mathbf{g}$  is the local gravitational acceleration,  $E$  is  $\rho \varepsilon + \rho u^2/2$ ,  $\varepsilon$  is the specific internal energy,  $P$  is the pressure, and  $q$  is the net heating and cooling. For gravity, we use the Newtonian monopole approximation,  $\mathbf{g} = -(GM/r^2)\hat{r}$ , and for pressure, we use a relativistic-mean-field equation of state (Shen et al. 1998). As initial conditions for these simulations, we use the 15- $M_\odot$  progenitor model of Woosley & Weaver (1995).<sup>3</sup>

Following the prescription established in Murphy & Burrows (2008) and Nordhaus et al. (2010), we approximate neutrino heating and cooling with local prescriptions, i.e.

$$q = \mathcal{H} L_\nu \left( \frac{100 \text{ km}}{r} \right)^2 \left( \frac{T_\nu}{4 \text{ MeV}} \right)^2 - C \left( \frac{T}{2 \text{ MeV}} \right)^6 \text{ [erg/g/s]}, \quad (4)$$

where  $L_\nu$  is the luminosity of electron- or anti-electron-type neutrinos in units of  $10^{52}$  erg/s,  $T_\nu$  is the temperature of the neutrinos (which we set to 4 MeV for all runs),  $T$  is the local matter temperature, and the constants are  $\mathcal{H} = 1.544 \times 10^{20}$

<sup>2</sup>  $v_r$  is the radial velocity

<sup>3</sup> See Murphy & Burrows (2008) and Hanke et al. (2011) for representative accretion rate history curves.

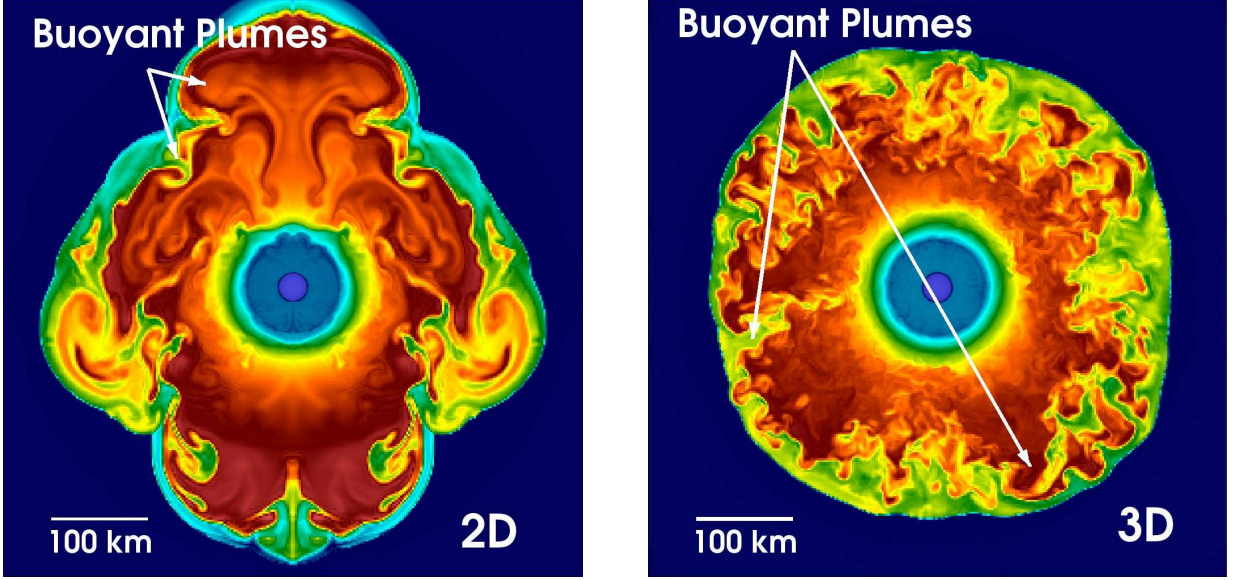


**Figure 1.** Entropy color maps of 2D (left) and 3D (right) CCSN simulations. Cooler colors represent lower entropies and warmer colors represent higher entropies. These stills represent the flow at 250 ms after bounce for  $L_\nu = 2.1 \times 10^{52}$  erg/s. The 2D simulation has a higher proportion of coherent structures, which turbulence theory predicts (Boffetta & Ecke 2012). Despite the differences between 2D and 3D, both show positively (high entropy) and negatively (low entropy) buoyant plumes, a strong indication of neutrino-driven convection.

and  $C = 1.399 \times 10^{20}$ . For a derivation of these constants see Janka (2001). In this paper, we consider neutrino luminosities of  $L_\nu = 2.1, 2.23$ , and  $2.3$ .

Absorption and emission of electron- and anti-electron-type neutrinos is most efficient on free protons and neutrons. Therefore, we weight the heating and cooling terms by the combined mass fractions of protons and neutrons, i.e.  $Y_p + Y_n$ . Equation 4 is an approximation that is most relevant in the optically-thin regime. Therefore, to suppress unphysical heating and cooling at high optical depths, we further weight eq. (4) by  $\exp(-\tau)$ , where  $\tau = \int \kappa \rho dr$  is an average optical depth of the electron- and anti-electron-type neutrinos,  $\kappa$  is the neutrino opacity, and we approximate the optical depth with

$$\tau = \frac{3}{4} \times 10^{-7} \left( \frac{T_\nu}{4 \text{ MeV}} \right)^2 \int (Y_n + Y_p) \left( \frac{\rho}{10^{10} \text{ g/cm}^3} \right) dr \quad (5)$$

To simulate the range in length and time scales encountered in core-collapse simulations, we use CASTRO's adaptive-mesh-refinement (AMR) and adaptive time-stepping capabilities. We have developed an AMR strategy to simulate the full dynamic range of spherical collapse, while keeping the run-time and memory requirements as low as possible. Overall, we use 6 levels of refinement, each a factor of two smaller than the next largest level. The largest domain of the 3D simulations is a cube with 10,000 km on a side and has a resolution of 32 km at the coarsest level. To adequately resolve the proto-neutron star (PNS) structure, the finest level has a resolution of  $\sim 0.5$  km out to a radius of 50 km. In between, we initialize the refinement level ( $\ell$ ) to maintain a roughly constant angular resolution of  $\Delta\theta \sim 0.7^\circ$ , i.e.

$$\ell_{\min} = \max \left( \min \left\{ \left\lfloor \log_2 \left( 64 \left[ \frac{40 \text{ km}}{r} \right] \right) \right\rfloor, 6 \right\}, 0 \right), \quad (6)$$

where  $\lfloor \cdot \rfloor$  is the floor function.

Throughout the simulation, we maintain eq. (6) as the minimum resolution. In addition, we set the minimum refinement level to 4 everywhere the entropy is greater than  $5 k_b/\text{baryon}$

(where  $k_b$  is Boltzmann's constant). Effectively, this extends level 4 refinement ( $\sim 2$  km resolution) to include all regions interior to the stalled shock. As the shock expands during explosion, level 4 refinement expands in radius requiring ever greater memory. To limit the storage requirements of the simulation we impose maximum radii for each refinement level via

$$\ell_{\max} = \max \left( \min \left\{ \left\lfloor \log_2 \left( 64 \left[ \frac{75 \text{ km}}{r} \right] \right) \right\rfloor, 6 \right\}, 0 \right). \quad (7)$$

### 3. RELEVANT ELEMENTS OF TURBULENCE THEORY

Using Reynolds decomposition, Murphy & Meakin (2011) developed a consistent set of equations for the evolution of the post-shock flow, including the effects of buoyant-driven convection. Here, we highlight elements of this turbulence theory that can be easily compared with the properties of the 3D simulations.

Including the effects of turbulence, the steady-state, spherically-averaged conservation equations for mass, momentum, and entropy are

$$\nabla \cdot (\rho_0 \mathbf{v} + \langle \rho' \mathbf{v}' \rangle) = 0, \quad (8)$$

$$\langle \rho \mathbf{u} \rangle \cdot \nabla \mathbf{v} = -\nabla P_0 + \rho_0 \mathbf{g} - \nabla \cdot \langle \rho \mathbf{R} \rangle \quad (9)$$

and

$$\langle \rho \mathbf{u} \rangle \cdot \nabla s_0 = \left\langle \frac{\rho q}{T} \right\rangle + \frac{\rho_0 \epsilon}{T_0} - \nabla \cdot \langle \mathbf{F}_s \rangle. \quad (10)$$

where  $\langle \cdot \rangle$  is an average over solid angle and approximately one eddy turn-over time, the subscript 0 denotes the background flow and the prime denotes the perturbation due to convection, and  $\epsilon$  is the turbulent dissipation. To avoid cumbersome subscripts later, we do not use 0 for the background velocity. Rather, the background velocity is  $\mathbf{v}$  and the perturbed velocity is  $\mathbf{v}'$ , i.e.  $\mathbf{u} = \mathbf{v} + \mathbf{v}'$ . The Reynolds-averaged equations are similar in form to the usual equations of hydrodynamics, except these equations have three new terms that are associated with turbulence. The mass equation, eq. (8),



includes the divergence of the buoyancy flux,  $\langle \rho' v' \rangle$ , the momentum equation includes the divergence of Reynolds stress<sup>4</sup>,  $\mathbf{R} = v'_i v'_j$ , and the entropy equation includes the transport of entropy by the turbulent entropy flux,  $F_s$ . For low-mach-number flows, the buoyant flux and entropy flux can be related by a thermodynamic derivative (Murphy & Meakin 2011), so in the rest of this paper, we consider only  $\mathbf{R}$  and  $F_s$ .

The new turbulent terms require additional equations to close the system of equations. See Murphy & Meakin (2011) for the full set, but here we discuss only the equation for  $\mathbf{R}$ , or more specifically, we present the specific kinetic energy ( $K$ ) equation, where  $K$  is related to the trace of the Reynolds stress by  $K = (1/2)\text{Tr}(\mathbf{R})$ . The turbulent kinetic energy equation<sup>5</sup> is

$$\begin{aligned} \partial \langle \rho K \rangle / \partial t + \mathbf{v} \cdot \nabla \langle \rho K \rangle + \langle \rho K \rangle \nabla \cdot \mathbf{v} = \\ + \langle \rho' v' \rangle \cdot \mathbf{g} - \nabla \cdot \langle \mathbf{F}_K \rangle - \nabla \cdot \langle \mathbf{F}_P \rangle \\ + \langle \mathbf{P}' \nabla \cdot \mathbf{v}' \rangle - \rho_0 \epsilon. \end{aligned} \quad (11)$$

On the right-hand-side of this equation, we have the work done by buoyancy, turbulent redistribution by the turbulent kinetic energy flux, the divergence of the pressure flux ( $\mathbf{F}_P = \mathbf{P}' \mathbf{v}'$ ), work done by turbulent pressure, and turbulent dissipation. For low-mach-number flows the pressure flux and work done by turbulent pressure are small, so henceforth we ignore these terms.

Assuming steady-state and integrating over the entire convective volume, we find a balance between global buoyant driving and global turbulent dissipation:

$$\int \langle \rho' v' \rangle \cdot \mathbf{g} dV = \int \rho_0 \epsilon dV, \quad (12)$$

where we assume zero turbulent kinetic energy flux at the boundaries of convection. In comparing this equation with 3D simulations, calculating the integrated buoyant driving term ( $W_b$ ) is trivial. We merely use the simulations to calculate the integral,  $W_b = \int \langle \rho' v' \rangle \cdot \mathbf{g} dV$ . Turbulent dissipation,  $E_k = \int \rho_0 \epsilon dV$ , on the other hand requires a model. We adopt Kolmogorov's hypothesis, in which dissipation is set by the largest scales<sup>6</sup> and is of order  $\epsilon \sim v'^3 / \mathcal{L}$ , where  $v'$  is a typical turbulent velocity on the largest length scale,  $\mathcal{L}$ . Formally,  $\mathcal{L}$  is a free parameter of the model. However, simulations of stellar models (Arnett et al. 2009) and core collapse (Murphy & Meakin 2011) indicate that  $\mathcal{L}$  takes on the largest possible value, the radial extent of the region actively driving convection. For this paper, we find that setting  $\mathcal{L}$  to the size of the gain region satisfies global balance. In effect,  $\mathcal{L}$  is no longer a free parameter, but a condition imposed by the global structure. If the post-shock turbulence is driven by buoyancy, then the 3D simulations should be consistent with eq. (12). In section 4, we show that the 3D simulations are indeed consistent with eq. (12).

Next, we derive analytic relationships for neutrino-driven convection. First, we use the entropy equation, eq. (10), to derive a scaling for the turbulent luminosity,  $T_0 L_s$ , where

<sup>4</sup> For practical purposes, we calculate  $R$  via  $\langle \rho v_i v'_j \rangle / \rho_0$ , which we find to be nearly identical to the definition given in the main text. Note, we could have easily defined  $R$  as  $\rho_0 v'_i v'_j$ . However, this definition obscures the behavior of the turbulent velocities with a steep density gradient.

<sup>5</sup> Note that there is an erroneous extra term in eq. (8) of Murphy & Meakin (2011). We have corrected it in this reproduction of the equation.

<sup>6</sup> Actually, the idea that dissipation starts at the largest scales and cascades to smaller scales was first proposed by Richardson (1922), but Kolmogorov (1941) established the quantitative theory that we reference in this paper.

$L_s = 4\pi r^2 F_s$ . In the convective region, we assume that the terms on the right-hand-side of the entropy equation, eq. (10), are of the same order. In the limit of a zero entropy gradient (efficient convection) or zero background velocity, the terms on the right-hand-side exactly balance. Even when the background velocity or entropy gradient is nonzero, we expect the terms on the right-hand-side to be of the same order. Under this assumption, we expect convective entropy redistribution ( $\nabla \cdot F_s$ ) to scale with neutrino heating ( $\rho q / T$ ). In other words,  $T_0 \partial L_s / \partial r \sim 4\pi r^2 \rho q$ . To express this in terms of  $L_\nu$ , we substitute the expression for  $q$  (eq. 4) into this expression, and assume that cooling is negligibly small in the heating region. Because the heating term is proportional to  $L_\nu \kappa / r^2$ , we arrive at  $T_0 \partial L_s / \partial r \sim L_\nu \kappa \rho$ , where  $\kappa$  is the opacity to neutrinos. A rough integration of this last scaling leads to

$$T_0 L_s \sim L_\nu \tau. \quad (13)$$

Therefore, if neutrino-driven convection dominates the turbulent motions, then we expect the turbulent luminosity,  $T_0 L_s$ , to be linearly dependent on the driving neutrino power, i.e. the neutrino luminosity times the neutrino optical depth in the gain region,  $L_\nu \tau$ . In section 4, we show that 3D simulations are consistent with this prediction.

For the second analytic scaling, we show that the turbulent dissipation also roughly scales linearly with the driving neutrino power. Equation (12) indicates a direct correlation between the scale of the buoyant flux,  $\langle \rho' v' \rangle$ , and the total turbulent dissipation,  $E_k = \int \rho_0 \epsilon dV$ . The buoyant flux can be related to the turbulent entropy flux,  $F_s$ , through a simple thermodynamic derivative, i.e.  $\langle \rho' v' \rangle \approx \eta F_s$ , where  $\eta = (\partial \rho / \partial s)_P / \rho$  is evaluated at constant pressure. Hence, total turbulent dissipation scales with  $F_s$ . Furthermore, virial arguments suggest a relationship between gravity and the thermal energy, e.g.  $GM/r \sim k_B T$ . Inserting these two scalings into eq. (12) and dropping  $k_B \eta$  (which is dimensionless), we have that  $T_0 L_s \sim E_k$ . This is not a new result, but just an approximate reiteration that buoyant driving is balanced by total turbulent dissipation. However, this approximate form, combined with the scaling derived for  $T_0 L_s$  in eq. (13), leads to a linear scaling between the total turbulent dissipation and the driving neutrino power, i.e.

$$E_k \sim L_\nu \tau. \quad (14)$$

Of these two predicted scalings, the one for  $T_0 L_s$  (eq. 13) relies on fewer approximations and is more fundamental. In essence, the two independent predictions of buoyancy-driven convection theory are that the turbulent luminosity,  $T_0 L_s$ , scales linearly with the driving neutrino power,  $L_\nu \tau$ , and that global buoyant driving is balanced by turbulent dissipation. The scaling for  $E_k$  (eq. 14), is merely a recasting of these two statements. Because eq. (14) is secondary, it necessarily requires more approximations. Despite these failings it is still informative to see how the dissipation scales with the driving neutrino power. So for completeness, we compare eq. (14) with 3D simulations in section 4, but we are more confident in the derivation of eq. (13), and therefore, we emphasize the linear scaling between turbulent luminosity and neutrino power.

An important aspect of the core collapse problem is the presence of the standing accretion shock, so we also consider how buoyancy-driven convection affects the stalled shock radius. Formally, the stalled shock is located where the upstream and the downstream profiles satisfy the Rankin-Hugoniot jump conditions. For zero shock velocity, the mass

flux, momentum flux, and energy flux conditions are

$$\Delta[\rho v] = 0, \quad (15)$$

$$\Delta[P + \rho v^2] = 0, \quad (16)$$

and

$$\Delta[\varepsilon + P/\rho + v^2/2] = 0. \quad (17)$$

In detail, the shock position is a nontrivial solution to a boundary value problem for  $\rho$ ,  $v$ , and  $P$ . However, with a few reasonable approximations, the shock boundary condition can be reduced to one expression. First, we assume steady-state and that the mass accretion rate ( $\dot{M}$ ) is constant. Secondly, we assume that the upstream flow is in near free-fall and essentially pressureless. Thirdly, we assume for the purposes of this argument that the equation of state is approximated by a  $\gamma$ -law, i.e.  $P = (\gamma - 1)\rho\varepsilon$ . The first and second assumptions completely determine the upstream flow as a function of radius. Because the upstream flow is pressureless, we use the strong shock limit to determine the shock compression ratio, i.e.  $\rho_d/\rho_u \approx (\gamma + 1)/(\gamma - 1)$ . Under these assumptions, the full Rankine-Hugoniot jump conditions reduce to a single expression:

$$P_d = \rho_u v_u^2 \left( 1 - \frac{\rho_u}{\rho_d} \right) \quad (18)$$

where  $u$  ( $d$ ) denotes upstream (downstream) state variables. Since the term in parentheses is  $\sim 1$ , the shock conditions reduce to an expression that demands a balance between the upstream ram pressure and the downstream thermal pressure. In essence, the primary independent shock condition is the momentum jump condition (eq. 16). From here on, we focus on the momentum jump condition with zero pressure on the upstream side, i.e.

$$P_d + \rho_d v_d^2 \approx \rho_u v_u^2. \quad (19)$$

Including turbulent pressure, the momentum jump condition becomes

$$P_d + \rho_d v_d^2 + \rho_d R_{rr} \approx \rho_u v_u^2, \quad (20)$$

where the velocities,  $v_d$  and  $v_u$ , are background velocities. Hence, the new shock position is located where the post-shock thermal, ram, and turbulent ram pressures balance the pre-shock ram pressure. The addition of the turbulent ram pressure likely results in larger shock radii.

Equation (20) by itself is not enough to determine the shock position. One must also specify the pre-shock and post-shock profiles, and it is the intersection of these profiles that determines the shock radius. The pre-shock ram pressure is given by free-fall assumptions, resulting in a fixed, relatively shallow profile (e.g.  $\rho_u v_u^2 \propto r^{-5/2}$ ). The post-shock region is in sonic contact and in rough hydrostatic equilibrium, so the postshock pressure depends upon physics (such as cooling) of the entire postshock region. Fortunately, though, the post-shock pressure profile can be expressed by a simple power-law (e.g.  $P \propto r^{-(3-4)}$ ), where the normalization depends upon the details of cooling, etc.. In section 4, we fit power-laws to the pre-shock and post-shock profiles of 3D simulations and use eq. (20) to predict the average shock radius with and without turbulent ram pressure. We calculate the correct average shock radius only if we include the turbulent ram pressure.

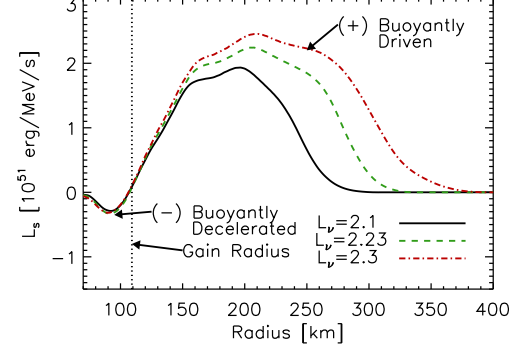


**Figure 2.** Turbulent entropy luminosity,  $L_s = 4\pi r^2 \langle F_s \rangle$  vs. radius at 250 ms after bounce for three driving neutrino luminosities ( $L_\nu = 2.1, 2.23$ , and  $2.3 \times 10^{52}$  erg/s). In general, these profiles are consistent with a neutrino-driven convection hypothesis.  $L_s$  is positive in the gain region where buoyancy actively drives convection, and it is negative where stabilizing entropy gradients cause buoyant deceleration. As is expected for neutrino-driven convection, the magnitude of the turbulent luminosity monotonically increases with the driving neutrino luminosity.

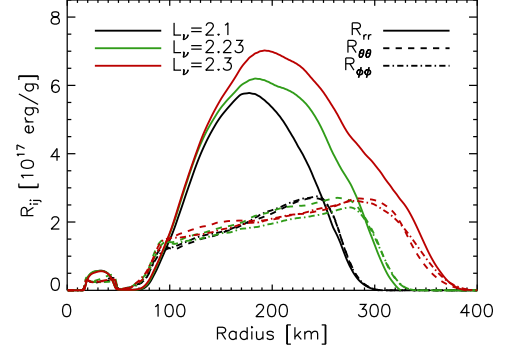


**Figure 3.** Reynolds stress as a function of radius and driving neutrino luminosity at 250 ms after bounce. All three diagonal components are shown: solid lines correspond to  $R_{rr}$ , dashed lines correspond to  $R_{\theta\theta}$ , dot-dashed lines correspond to  $R_{\phi\phi}$ . On average,  $R_{rr} \sim R_{\theta\theta} + R_{\phi\phi}$  globally, and  $R_{\phi\phi} \approx R_{\theta\theta}$  locally. This equipartition in kinetic energy between the radial and tangential components is a commonly observed feature in buoyancy-driven convection, and is a consequence of buoyant driving in the radial direction, redistribution to the tangential components, and turbulent dissipation among all of the components. As is expected for neutrino-driven convection,  $R_{rr}$  increases with neutrino luminosity.

#### 4. RESULTS

In this section, we present many ways in which 3D CCSN simulations are consistent with the hypothesis that neutrino-driven convection dominates the multi-dimensional motions. Figure 2 shows the turbulent entropy luminosity,  $L_s = 4\pi r^2 F_s$ , versus radius for 3 different driving neutrino luminosities at 250 ms after bounce. The gross features of these profiles are consistent with buoyancy-driven convection. In particular,  $L_s$  is positive where convection is actively driven by heating in the gain region, and  $L_s$  is negative where convective plumes overshoot into the cooling region and are decelerated by stabilizing entropy gradients. Furthermore, the magnitude of  $L_s$  monotonically increases with the driving neutrino luminosity, an expected result for neutrino-driven convection.

Similarly, neutrino-driven convection explains the Reynolds stresses. In Figure 3, we plot the radial ( $R_{rr}$ , solid line) and tangential components ( $R_{\theta\theta}$  and  $R_{\phi\phi}$ , dashed and dot-dashed lines) of the Reynolds stress vs. radius at

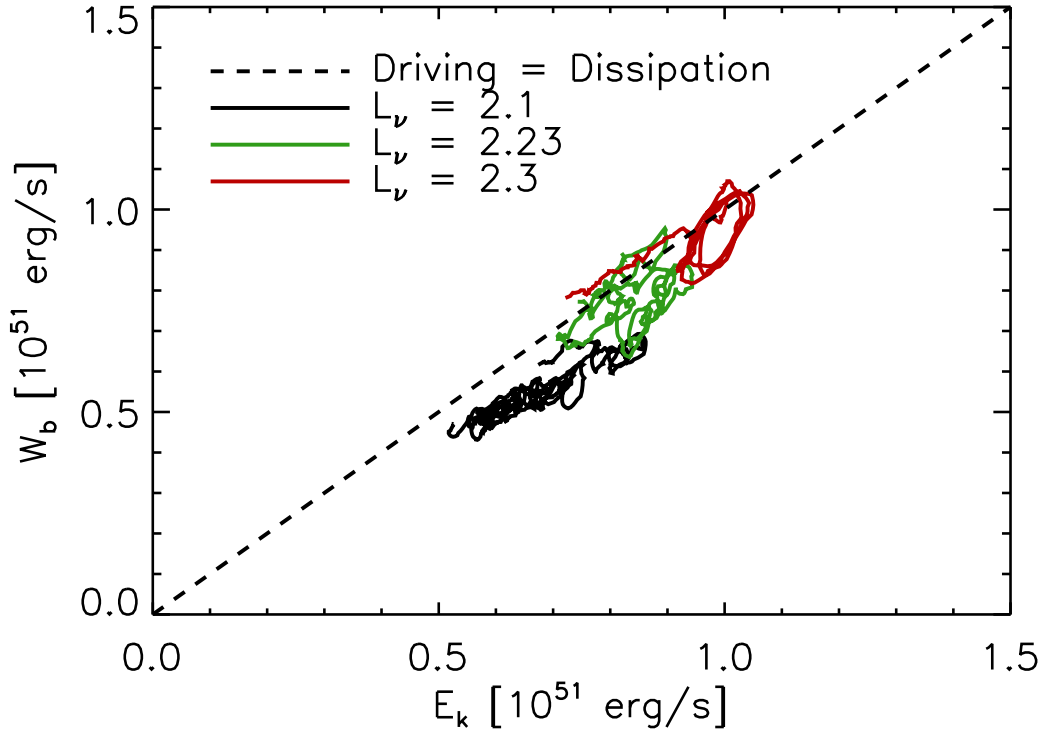


**Figure 4.** Global buoyant driving,  $W_b$ , vs. Global turbulent dissipation,  $E_k$ . The fact that buoyant driving equals turbulent dissipation as predicted by turbulence theory (Arnett et al. 2009; Garaud et al. 2010; Murphy & Meakin 2011) is a strong indicator that the neutrino-driven convection dominates the aspherical, nonlinear flow.

250 ms after bounce. Two characteristics of the profiles are consistent with buoyancy-driven convection. First, like  $L_s$ , the strength of the turbulent stresses (mostly  $R_{rr}$ ) increases monotonically with neutrino luminosity. Secondly, the radial component of the turbulent stress is approximately equal to the combined tangential components; i.e.  $R_{rr} \sim R_{\phi\phi} + R_{\theta\theta}$ . This result is consistently seen in other numerical experiments where turbulence is unambiguously driven by buoyancy (see Arnett et al. (2009), and references therein). In analytic derivations (Arnett et al. 2009; Garaud et al. 2010; Murphy & Meakin 2011), this approximate equipartition arises because buoyancy acts first on the radial component, and then the turbulence is dissipated after energy is redistributed among the three components.

A prediction of the turbulent kinetic energy equation (eq. 11) is that, globally, buoyant driving is balanced by turbulent dissipation (eq. 12). Figure 4 validates this prediction. In this plot, we show global buoyant driving,  $W_b$ , vs. global turbulent dissipation,  $E_k$ , for several driving neutrino luminosities. In summary, Figure 4 verifies that  $W_b \propto \int \rho R_{rr}^{3/2} dV$ , that the constant of proportionality is the largest scale as predicted by Kolmogorov, and that global buoyant driving balances global turbulent dissipation.

In section 3, we argue that the convective luminosity,  $T_0 L_s$ , and turbulent dissipation,  $E_k$ , scale linearly with the driving neutrino-power,  $L_{\nu}\tau$ . Figures 5 and 6 compare these analytic scalings, eqs. (13-14), (dotted lines) with the results from the 3D simulations (diamonds). Indeed, both the turbulent luminosity (Figure 5) and turbulent dissipation (Figure 6) are linearly proportional to the driving neutrino power. To calculate the constant of proportionality, we merely report the ratio of

the luminosities at the last points. Coincidentally, the constants of proportionality,  $\alpha$  and  $\beta$ , approximately sum to one. From this coincidence, one might be tempted to conclude that  $T_0 L_s + E_k \sim L_{\nu}\tau$ . However, this supposition would contradict global balance of driving and dissipation which is a firm theoretical prediction. Rather, we suspect that this interesting coincidence is merely a consequence of the approximate derivations leading to these scalings. Other than the fact that these constants are of order unity, we put no real emphasis on their values. The main result is that turbulence scales linearly with neutrino power, as is expected in buoyant convection.

Finally, we find that turbulent ram pressure explains in part the expansion of the shock radius. As we argue in section 3, the position of the shock radius is essentially determined where the pre-shock ram-pressure profile and the post-shock pressure profiles satisfy the momentum jump condition (eq. 20). In essence, the shock radius is established where the ram pressure of the upstream flow is balanced by the thermal, ram, and turbulent pressure of the downstream flow (see eqs. (19-20) and the surrounding text in section 3). Figure 7 shows for one representative neutrino luminosity fits to the upstream ram pressure (dotted line) and downstream thermal, ram, and turbulent pressures (solid line), as a function of radius. Using these pressure profiles, we calculate the shock to be located where the upstream and downstream fits cross. To identify where the shock would be without the turbulent pressure, we construct similar models for the downstream flow that exclude the turbulent pressure. For comparison we show the actual average shock radius ( $\langle R_s \rangle$ ) from a 3D simulation (dot-dot-dot-dashed line). Without the turbulent ram pressure, the calculated shock radius is  $\sim 40$  km short of the actual av-

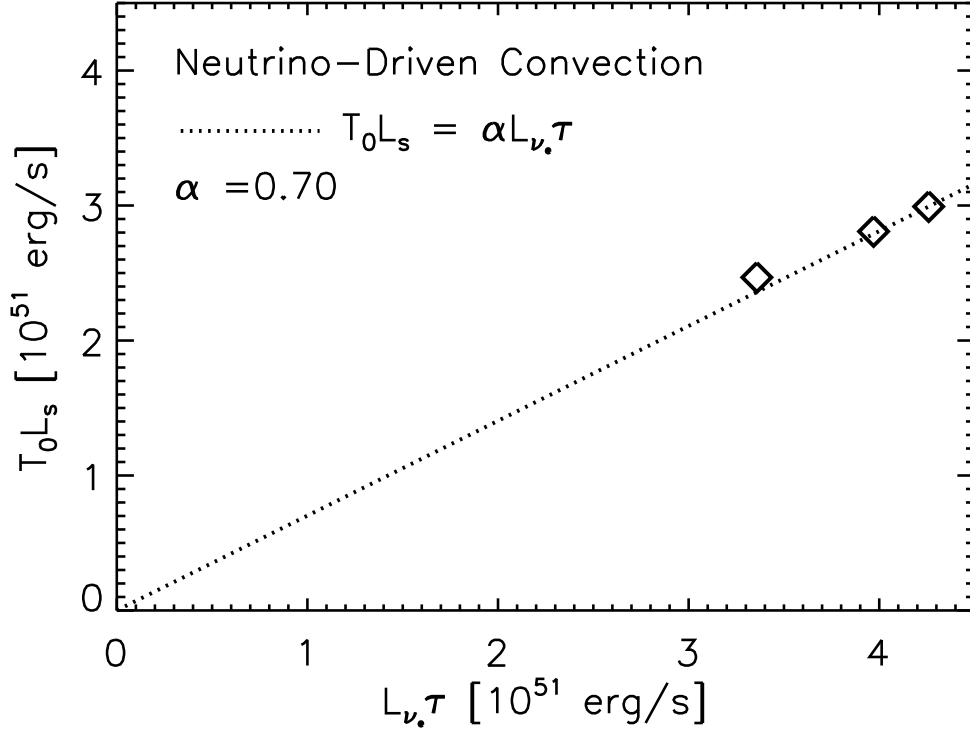


**Figure 5.** Convective luminosity ( $T_0 L_s$ ) vs. the driving neutrino power,  $L_{\nu_e} \tau$ . The symbols show the maximum value of  $T_0 L_s$  (restricted to the gain region) for three 3D simulations, all at 250 ms after bounce. For neutrino-driven convection, we analytically expect this convective luminosity to be linearly proportional to the driving neutrino power. For comparison, the dashed line shows this linear expectation. Our analytic calculation does not determine the constant of proportionality, so using the 3D simulations, we find that  $\alpha \sim 0.7$ . See eq. (13) and the associated text for the derivation of the analytic scalings with neutrino luminosity.

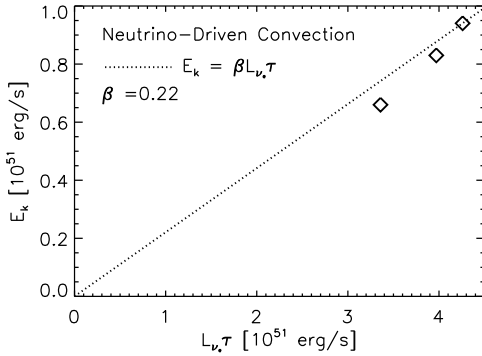


**Figure 6.** Turbulent dissipation rate,  $E_k$ , vs. the driving neutrino power,  $L_{\nu_e} \tau$ . Similar to Figure 5, the diamonds show the 3D simulation results and the dashed line shows the expected linear scaling with driving neutrino power, eq. (14). More approximations are involved in deriving eq. (14), so the scaling in this plot is less robust than the scaling in Figure 5. Nonetheless, this plot shows that turbulent dissipation is roughly proportional to the driving neutrino power, as is expected for neutrino-driven convection.

erage shock radius, but when we include the turbulent ram pressure, we accurately calculate the shock radius.

Figure 8 shows the resulting shock locations as a function of driving neutrino luminosity. This plot shows the modeled shock radii, including turbulent ram pressure (solid line) and the modeled shock radii excluding turbulent ram pressure (dashed line). For comparison, we show the calculated minimum (triangles), average (diamonds), and maximum (squares) shock radii for 3D simulations all at 250 ms

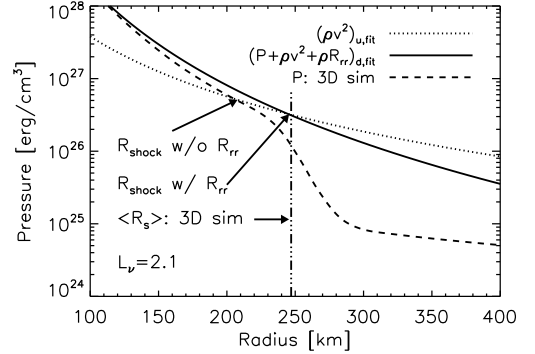


**Figure 7.** Upstream (u) and downstream (d) momentum terms in the momentum shock condition, eq. (20), and the resulting shock position. In essence, the average shock radius is established where the ram pressure of the upstream flow (dotted line) balances the thermal, ram, and turbulent ram pressure of the downstream flow (solid line). The solid and dotted lines are fits to their respective flows. The dashed line shows the average pressure from the 3D simulations. For comparison, we show the average shock radius ( $\langle R_s \rangle$ ) of the 3D simulation (dot-dot-dashed line). Neglecting the turbulent ram pressure, one would predict a smaller shock radius. The predicted and actual average shock radius is  $\sim 40$  km larger than it otherwise would be without the turbulent ram pressure. In Figure 8, we use these curves to calculate the location of the average shock radius for several neutrino luminosities and show that it is a monotonically increasing function of  $L_{\nu_e}$  and that turbulent pressure pushes the shock out to larger radii.

after bounce. Including turbulent pressure in the post-shock profile predicts shock radii that agree with the measured average shock radius. Excluding the turbulent pressure under-



predicts the average shock radius. On the other hand, excluding the turbulent pressure gives shock radius predictions that are consistent with the minimum shock radii. This suggests that the minimum shock radii occur at places and times where the fluctuating turbulent motions are instantaneously negligible. On average though, the turbulent motions are not negligible and influence the average shock radius.

Showing that turbulent ram pressure causes expansion of the shock radius does not by itself prove that buoyant-driven convection is responsible for the expansion. Any instability that leads to turbulence would give a similar prediction. However, the dependency of the shock radii and the turbulent pressure on  $L_{\nu_e}$  does strongly suggest the prominence of neutrino-driven convection.

## 5. CONCLUSIONS AND DISCUSSION

We have identified in section 4 five ways in which the aspherical, nonlinear flow of 3D CCSN simulations is consistent with buoyancy-driven convection theory. For one, the turbulent luminosity is positive in the gain region where buoyancy actively drives convection, and the turbulent luminosity is negative in the stably-stratified region where buoyancy decelerates convective plumes. Secondly, the radial component of the Reynolds stress is in rough equipartition with the tangential components, i.e.  $R_{rr} \sim R_{\theta\theta} + R_{\phi\phi}$ ; this result is observed in other contexts of buoyancy-driven convection and is expected when convection is driven radially, but dissipated among all the components (Arnett et al. 2009; Garaud et al. 2010; Murphy & Meakin 2011). Thirdly, we find that global turbulent dissipation is balanced by global buoyant driving. Fourthly, both the turbulent luminosity and turbulent dissipation scale linearly with the driving neutrino power, a result we derive from buoyant convection theory. Finally, we calculate a consistent solution for the average shock radius only if we include the turbulent ram pressure in the shock jump conditions. In essence, these results are consistent with the hypothesis that neutrino-driven convection is the dominant multi-dimensional instability in our 3D CCSN simulations.

These results also suggest that there is no need to invoke any other multi-dimensional instabilities, in particular the SASI, to explain the aspherical, nonlinear motions. Of course, our results do not prove that the SASI is absent. Rather, they suggest that the nonlinear motions are merely consistent with buoyant convection and that if the SASI is present it mimics buoyant convection, or is subdominant. Numerous analytic and numerical studies have shown that if the conditions are right, a nonlinear SASI arises. However, these studies were performed largely in the absence of neutrino heating. A few did include neutrinos, but as far as we can tell, neutrino-driven convection eventually dominates the flow of these simulations (Foglizzo et al. 2006; Scheck et al. 2008; Fernández & Thompson 2009). It appears that in attempting to isolate the SASI mechanism, researchers were suppressing the dominant nonlinear instability in core-collapse simulations.

Minimally, there are two hypotheses for the dominant multi-dimensional instability: the SASI and buoyancy-driven convection. Neither hypothesis can be proven; they can only be shown to be consistent or disproven. Because a self-consistent theory exists for nonlinear, buoyant convection (e.g. Murphy & Meakin 2011), we can show that buoyancy-driven convection is consistent with post-shock turbulence. However, there is as yet no self-consistent theory for a nonlinear SASI mechanism, so we can not test the SASI at this

time. In fact, it is entirely possible that some aspects of nonlinear convection theory would be mirrored in a nonlinear SASI theory. For example, in both cases, turbulence is most likely dissipated in accord with Kolmogorov’s hypothesis. However, we have shown that turbulent dissipation is balanced by buoyant driving, which seems an unlikely prediction of a nonlinear SASI theory. In any case, it is clear that a nonlinear theory for the SASI must be developed before we can definitively claim that the SASI is subdominant. Furthermore, even though our approximations are designed to closely mimic more self-consistent simulations, a robust conclusion on the importance of convection must wait for full 3D neutrino-transport hydrodynamic simulations.

In the meantime, we have shown that a theory for nonlinear, buoyant convection is consistent with the post-shock turbulence of 3D simulations that include neutrino heating. Not surprisingly, we find that neutrino-driven convection accompanies neutrino-driven explosions.

## ACKNOWLEDGMENTS

The authors acknowledge stimulating interactions with Jason Nordhaus, Ann Almgren, and Thomas Janka. A.B. is supported by the Scientific Discovery through Advanced Computing (SciDAC) program of the DOE, under grant number DE-FG02-08ER41544, the NSF under the subaward no. ND201387 to the Joint Institute for Nuclear Astrophysics (JINA, NSF PHY-0822648), and the NSF PetaApps program, under award OCI-0905046 via a subaward no. 44592 from Louisiana State University to Princeton University. The authors would like to thank the members of the Center for Computational Sciences and Engineering (CCSE) at LBNL for their invaluable support for CASTRO. The authors employed computational resources provided by the TIGRESS high performance computer center at Princeton University, which is jointly supported by the Princeton Institute for Computational Science and Engineering (PICSciE) and the Princeton University Office of Information Technology; by the National Energy Research Scientific Computing Center (NERSC), which is supported by the Office of Science of the US Department of Energy under contract DE-AC03-76SF00098; and on the Kraken supercomputer, hosted at NICS and provided by the National Science Foundation through the TeraGrid Advanced Support Program under grant number TG-AST100001.

## REFERENCES

- Almgren, A. S., Beckner, V. E., Bell, J. B., Day, M. S., Howell, L. H., Joggerst, C. C., Lijewski, M. J., Nonaka, A., Singer, M., & Zingale, M. 2010, *ApJ*, 715, 1221
- Arnett, D., Meakin, C., & Young, P. A. 2009, *ApJ*, 690, 1715
- Bazan, G., & Arnett, D. 1998, *ApJ*, 496, 316
- Benz, W., Colgate, S. A., & Herant, M. 1994, *Physica D Nonlinear Phenomena*, 77, 305
- Bethe, H. A. 1990, *Reviews of Modern Physics*, 62, 801
- Bethe, H. A., & Wilson, J. R. 1985, *ApJ*, 295, 14
- Blondin, J. M., & Mezzacappa, A. 2006, *ApJ*, 642, 401
- Blondin, J. M., Mezzacappa, A., & DeMarino, C. 2003, *ApJ*, 584, 971
- Boffetta, G., & Ecke, R. E. 2012, *Annu. Rev. Fluid Mech.*, 427
- Buras, R., Rampp, M., Janka, H.-T., & Kifonidis, K. 2003, *Physical Review Letters*, 90, 241101
- Burrows, A. 1987, *ApJ*, 318, L57
- Burrows, A., Dessart, L., & Livne, E. 2007, in *American Institute of Physics Conference Series*, Vol. 937, *Supernova 1987A: 20 Years After: Supernovae and Gamma-Ray Bursters*, ed. S. Immler & R. McCray, 370–380
- Burrows, A., Dolence, J. C., & Murphy, J. W. 2012, *ArXiv e-prints*
- Burrows, A., Hayes, J., & Fryxell, B. A. 1995, *ApJ*, 450, 830



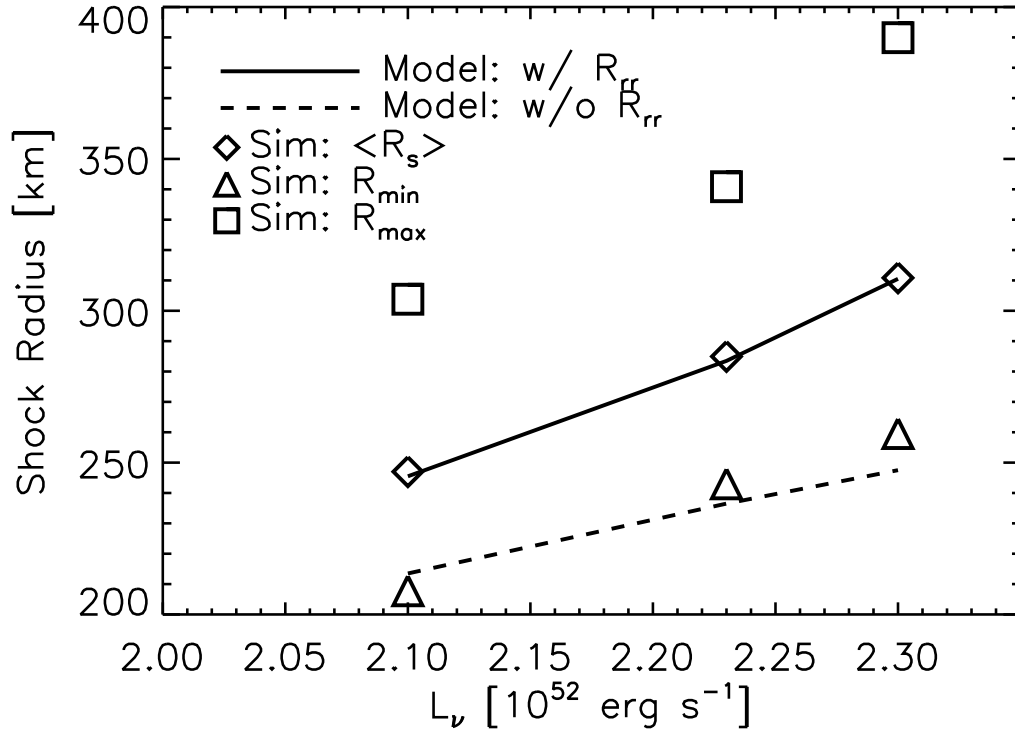


**Figure 8.** Simulated and calculated shock radii, with and without turbulent ram pressure at 250 ms after bounce. We plot the average (diamonds), minimum (triangles), and maximum (squares) shock radii versus neutrino luminosity. Using the average pre- and post-shock thermal and momentum pressure profiles (Figure 7), we calculate the expected shock radius with and without turbulent pressure. Including the turbulent ram pressure gives a larger shock radius and matches the average shock radius from the simulations. Calculations of the shock radii that exclude the turbulent ram pressure match the minimum shock radii of the 3D simulations.

- Epstein, R. I. 1979, MNRAS, 188, 305  
 Fernández, R. 2010, ApJ, 725, 1563  
 Fernández, R., & Thompson, C. 2009, ApJ, 703, 1464  
 Foglizzo, T. 2009, ApJ, 694, 820  
 Foglizzo, T., Masset, F., Guilet, J., & Durand, G. 2012, Physical Review Letters, 108, 051103  
 Foglizzo, T., Sheck, L., & Janka, H.-T. 2006, ApJ, 652, 1436  
 Garaud, P., Ogilvie, G. I., Miller, N., & Stellmach, S. 2010, MNRAS, 407, 2451  
 Guilet, J., & Foglizzo, T. 2012, MNRAS, 421, 546  
 Hanke, F., Marek, A., Mueller, B., & Janka, H.-T. 2011, ArXiv e-prints  
 Herant, M., Benz, W., & Colgate, S. 1992, ApJ, 395, 642  
 Herant, M., Benz, W., Hix, W. R., Fryer, C. L., & Colgate, S. A. 1994, ApJ, 435, 339  
 Janka, H.-T. 2001, A&A, 368, 527  
 Janka, H.-T., & Müller, E. 1995, ApJ, 448, L109  
 —. 1996, A&A, 306, 167  
 Kitaura, F. S., Janka, H.-T., & Hillebrandt, W. 2006, A&A, 450, 345  
 Kolmogorov, A. N. 1941, Dokl. Akad. Nauk SSSR, 299  
 Liebendörfer, M., Mezzacappa, A., & Thielemann, F.-K. 2001a, Phys. Rev. D, 63, 104003  
 Liebendörfer, M., Mezzacappa, A., Thielemann, F.-K., Messer, O. E., Hix, W. R., & Bruenn, S. W. 2001b, Phys. Rev. D, 63, 103004  
 Liebendörfer, M., Rampp, M., Janka, H.-T., & Mezzacappa, A. 2005, ApJ, 620, 840  
 Marek, A., & Janka, H. . 2007, ArXiv e-prints, 708  
 Meakin, C. A., & Arnett, D. 2007, ApJ, 665, 690  
 Murphy, J. W., & Burrows, A. 2008, ApJ, 688, 1159  
 Murphy, J. W., & Meakin, C. 2011, ApJ, 742, 74  
 Nordhaus, J., Burrows, A., Almgren, A., & Bell, J. 2010, ApJ, 720, 694  
 Rampp, M., & Janka, H.-T. 2002, A&A, 396, 361  
 Richardson, L. F. 1922, Weather Prediction by Numerical Process (Cambridge: Cambridge University Press)  
 Sato, J., Foglizzo, T., & Fromang, S. 2009, ApJ, 694, 833  
 Scheck, L., Janka, H.-T., Foglizzo, T., & Kifonidis, K. 2008, A&A, 477, 931  
 Shen, H., Toki, H., Oyamatsu, K., & Sumiyoshi, K. 1998, Nuclear Physics A, 637, 435  
 Thompson, T. A., Burrows, A., & Pinto, P. A. 2003, ApJ, 592, 434  
 Wilson, J. R., & Mayle, R. W. 1988, Phys. Rep., 163, 63  
 Woosley, S. E., & Weaver, T. A. 1995, ApJS, 101, 181  
 Yamasaki, T., & Yamada, S. 2006, ApJ, 650, 291